Aiming strategy model based on allowable flux densities for molten salt central receivers

Alberto Sánchez-González*, María Reyes Rodríguez-Sánchez, Domingo Santana

Universidad Carlos III de Madrid, Department of Thermal and Fluid Engineering, Av. de la Universidad, 30, 28911, Leganés, Madrid, Spain

*Corresponding author. Tel.: +34 916248884   E-mail address: asgonzal@ing.uc3m.es

Abstract

This study presents an aiming model to properly point heliostats at cylindrical molten salt receivers in Solar Power Tower. By means of two iterative algorithms –search and fit–, the proposed strategy attempts to maximize the receiver thermal power output while preserving the receiver operational limits. Corrosion and thermal stress constraints are translated into allowable flux densities (AFD) that are handled by the model. The computer code accommodates the flux images produced by each heliostat in a field to accurately fit the AFD limit. In this paper, a Gemasolar-like field-receiver system serves to illustrate the aiming model. Compared to the equatorial aiming, receiver interception is slightly lower using the proposed strategy, but the receiver integrity is ensured; peak flux is significantly reduced up to 23%. It has been found that a favorable flux density profile generally has its peak displaced to the salt entrance at each receiver panel. Since external cylindrical receivers consist of a combination of up-flow and down-flow panels, the optimal flux profile is challenging for contiguous panels with contrary demands. In spite of that, remarkable matching is achieved by the fit algorithm. Because of its fast computation and automatic operation, the resulting tool can be applied to real-time control of existing heliostat fields and the integrated design of the coupled systems field and receiver.

Keywords: Interaction field-receiver; Heliostat aim point; Iterative algorithm; Corrosion and thermal stress.

Nomenclature

A	difference between F and AFD profiles along the vertical [W/m]
AFD	allowable flux density [W/m^2]
BR_k	beam radius based on aiming factor [m]
Cp	specific heat [J/kg·K]
D	receiver diameter [m]
d	tube diameter [m]
DNI	direct normal irradiance [W/m^2]
E	modulus of elasticity [Pa]
F	solar flux density [W/m^2]
f	optical loss factor [–]

H	receiver height [m]
k	aiming factor [–]
$\dot{m}$	mass flow rate [kg/s]
N	number [–]
PW	panel width [m]
Q	heat rate [W]
q	heat flux density [W/m²]
r	row [–]
S	stress [Pa]
SLR	slant range [m]
T	temperature [ºC]
t	target vector
TC	thermal conductivity [W/m·K]
TE	coefficient of thermal expansion [m/m·K]
th	tube thickness [m]
THT	tower optical height [m]
TS	tensile strength [Pa]
UTS	ultimate tensile strength [Pa]
x, z	coordinates [m]

Greek symbols

ΔT_r	radial temperature difference [ºC]
ε	elevation angle [rad]
η	efficiency [–]
v	Poisson's ratio [–]
σ	error, standard deviation [rad]
ω	incidence angle [rad]

Subscripts

amb	ambient
conv	convection
corr	corrosion
e	effective
f	film
fp	flow path
i	inner tube surface
in	inlet
int	interception
j	index (iteration)
lim	limit
max	maximum, peak

o	outer tube surface
out	outlet
p	panel
r	row
rad	radiation
rec	receiver
s	molten salt
slp	mirror slope
strs	thermal stress
sun	sunshape
t	tube
trk	heliostat tracking

Abbreviations

CPU	central process unit
CRS	central receiver system
HTF	heat transfer fluid

1.   Introduction

In Central Receiver Systems, also called Solar Power Tower plants, thousands of heliostats concentrate sunlight at the central receiver (Vant-Hull, 2012). The interaction between heliostat field and thermal receiver plays an important role in the design and operation of Central Receiver Systems (CRS). Since single aiming usually leads to exceed the receiver technical limits, the development of multi-aiming strategies is fundamental.

Several researchers have recently developed aiming strategy models based on metaheuristic techniques. (Salomé et al., 2013) used a TABU algorithm to flatten the flux distribution on THEMIS flat plate receiver, while minimizing the spillage loss. (Besarati et al., 2014) addressed the same problem but employing a genetic algorithm (GA). An ant colony optimization (ACO) metaheuristic was adapted by (Belhomme et al., 2013) to maximize the electrical output of a concentrated photovoltaic receiver.

Other aiming approaches put the emphasis on meeting the operational limits of the receiver. (García-Martín et al., 1999) developed a closed-loop control algorithm for TSA volumetric receiver. Air temperature was measured at different points in the receiver, and then the algorithm adjusted the position of five aim points and the heliostat tracking in order to comply with the temperature limits.

(Vant-Hull, 2002) introduced the concept of allowable flux density (*AFD*) dependent on heat transfer fluid (HTF) temperature and flow rate, which was quantified for the cylindrical molten salt receiver at Solar Two plant. When overflux conditions were detected by RCELL code (Lipps and Vant-Hull, 1978), the dynamic aim processing system (DAPS) was responsible for: a) identifying the heliostats producing the greatest flux peak at the hot spots, and b) removing them from tracking. Given an outlet set point temperature, the receiver control

system consequently decreases the mass flow rate, which in turn lowers the *AFD* limit. Occasionally, numerous heliostats have to be removed from tracking, leading to instability (Pacheco, 2002).

In the present work, we have developed an alternative aiming approach based on the allowable flux density limit. The proposed model selects the heliostats' aim points that provide a good enough solution that attempts to maximize the thermal power output from a cylindrical molten salt receiver. To meet the goal, a recursive algorithm has been implemented. A general overview of the proposed aiming strategy model is given in the following section.

2.   General description

The objective of the proposed aiming strategy model is to point the heliostats in a way that looks for collecting as much as possible solar flux on the receiver while maintaining its structural integrity. In external cylindrical receivers, aim points are vertically shifted. Heliostat flux images superpose so that the whole flux map keeps within the allowable flux density limits. The inputs required by the aiming model are provided by an optical model and a database of allowable flux densities. These inputs are depicted in the general flowchart in Fig. 1, along with the initial input data: heliostat field configuration, receiver geometry, material properties and boundary conditions (i.e. solar time, *DNI*, and ambient temperature).
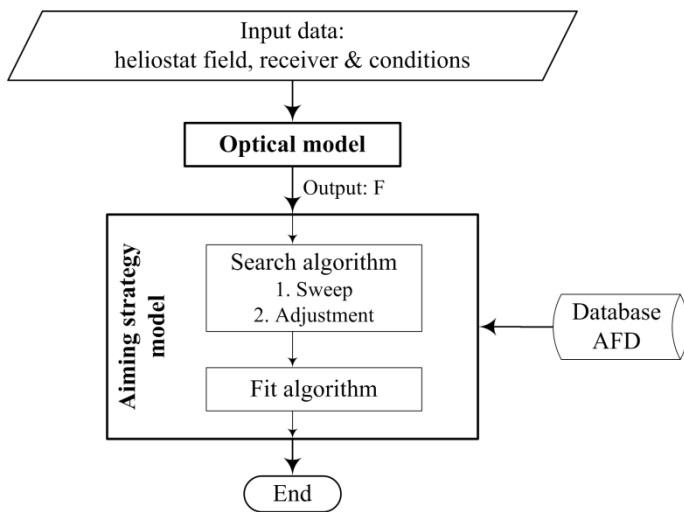

Fig. 1: General flowchart of the whole model.

The optical model previously validated by the authors (Sánchez-González and Santana, 2015) will be herein utilized. This model computes the flux density distribution caused by a whole field of heliostats, taking into account optical losses: shading, blocking, cosine, attenuation, reflectivity, and spillage. The basis of the model is on the oblique projection, from image plane into receiver surfaces, of the flux distribution predicted by an analytic function; in this instance UNIZAR function by (Collado et al., 1986). The effective error σ_e derives from the convolution of three circular Gaussian distributions: sunshape σ_{sun}, mirror slope error σ_{slp} and heliostat tracking error σ_{trk}, so that:

$$\sigma_e = \sqrt{\sigma_{sun}^2 + 2(1+\cos\omega)\sigma_{slp}^2 + \sigma_{trk}^2} \qquad (1)$$

where ω is the incidence angle of the solar beam on the heliostat. For a normal distribution, 99.7% of the reflected flux is within the angle subtended under $3\sigma_e$, 95% under $2\sigma_e$, and 68% under σ_e. Hence, a parameter typically ranging between 0 and 3, which is named aiming factor, is defined. In terms of the aiming factor k, the radius of the reflected beam (BR) on the receiver vertical, see Fig. 11a, can be estimated according to Eq. (2) for a given heliostat with slant range to the target point SLR and ε elevation angle of the reflected beam (i.e. target vector t). The concept of beam radius dependent on k aiming factor (BR_k) is crucial for the proposed aiming strategy model in order to control the spillage losses, as will be shown in algorithms section 5.

$$BR_k = \frac{k \cdot \tan\sigma_e \cdot SLR}{\cos\varepsilon} \approx \frac{k \cdot \sigma_e \cdot SLR}{\cos\varepsilon} \qquad (2)$$

On the other hand, the receiver must comply with some limitations in order to operate reliably and safely. The two main constraints are corrosion of metal tubes, and excessive thermal stress. Tube corrosion in the presence of high temperature molten salt can be prevented by limiting the maximum film temperature. Likewise, receiver failure can be avoided by reducing the thermal gradient on the tube.

Since the output parameter controlled by an aiming strategy is the flux distribution on the receiver, rather than film temperature or thermal gradient in the tubes, both restrictions (i.e. corrosion and thermal stress) are translated into a maximum allowable flux density (AFD) incident on the receiver. This approach, previously reported by (Vant-Hull, 2002) has been adopted in the model. For the corrosion constraint, such AFD depends on the HTF mass flow rate and temperature, which in turn depend on the receiver geometry: diameter D, height H, number of panels N_p, and tube diameter d. A detailed description of our methodology to generate a database of AFD is presented in section 4.

The proposed aiming model consists of two sequential algorithms, see Fig. 1. The objective of the first one – named search algorithm– is to find the maximum aiming factor with which the AFD limit could be accomplished using a symmetric aiming strategy with respect to the equator. Then, the fit algorithm is responsible for selecting the aim points so that the flux profiles match the AFD limit which is usually non-symmetric. In section 5 both algorithms are described.

In addition to the optical model of the heliostat field, a thermal model of the receiver is required to predict the heat exchange processes taking place in the central receiver. Such a receiver model is essential not only to generate the database of AFD, but also to calculate the mass flow and temperature of the HTF at different stages during the aiming strategy calculation procedure.

The receiver model previously reported by the authors (Rodríguez-Sánchez et al., 2014a, 2014b) will be herein utilized. This model considers temperature variations in both axial and circumferential directions; i.e. 2D discretization of the tubes. The heat flux absorbed by each cell is calculated by means of the Net Radiation

Method by (Modest, 2003), taking into account the view factors computed with the crossed-string method. The external convective heat coefficient is obtained from (Siebers and Kraabel, 1984). For any receiver design, the core of the model computes the heat fluxes and temperatures at each cell node, given an incident solar flux density distribution and a HTF mass flow rate. Setting the HTF temperatures at inlet and outlet, the model also recomputes the mass flow rate at each iteration, as shown in the receiver flowchart in Fig. 2 and according to the following equation.

$$\dot{m}_{s,new} = \frac{Q_{rec}}{Cp_s\left(T_{s,out} - T_{s,in}\right)} \tag{3}$$
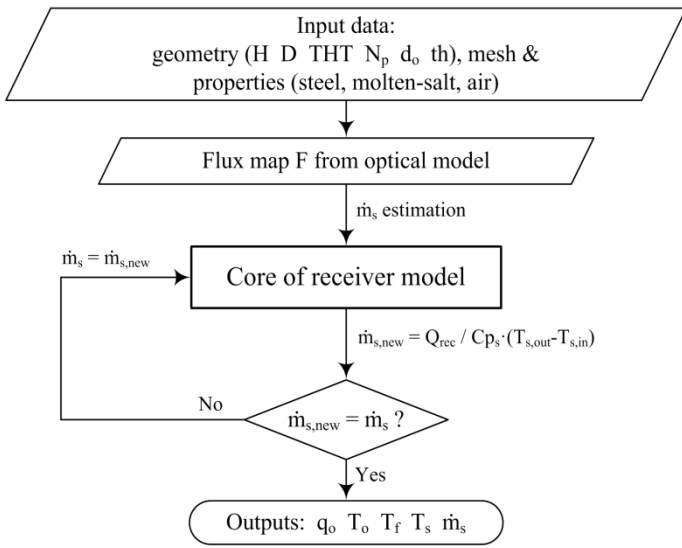

Fig. 2: Flowchart of the receiver model.

Prior to explaining the *AFD* database generation and the main algorithms in sections 4 and 5 respectively, the case study used throughout this paper is presented in the following section. Results for different solar times are exposed and discussed at the end of this manuscript.

3. Case study

The case study used throughout this paper is based on Gemasolar solar tower power plant located in Fuentes de Andalucía, Spain, at 37.56º north latitude. The heliostat field, biased to the north, consists of an inner radial cornfield zone and two outer staggered zones. The coordinates of the 2650 heliostats have been gathered through a scaled aerial photograph. The layout of Gemasolar field is shown in Fig. 3. The reflective area of the square heliostats is 115.7 m^2 (Lata et al., 2010). Mirror reflectivity and cleanliness are assumed to be 0.88 and 0.95, respectively. The sunshape standard deviation σ_{sun} is set to 2.51 mrad. Errors of mirror slope σ_{slp} and heliostat tracking σ_{trk} are assumed to be 2.6 and 2.1 mrad, even though this tracking error could be neglected for aiming strategy purpose where increasing the beam radius may not be plausible.
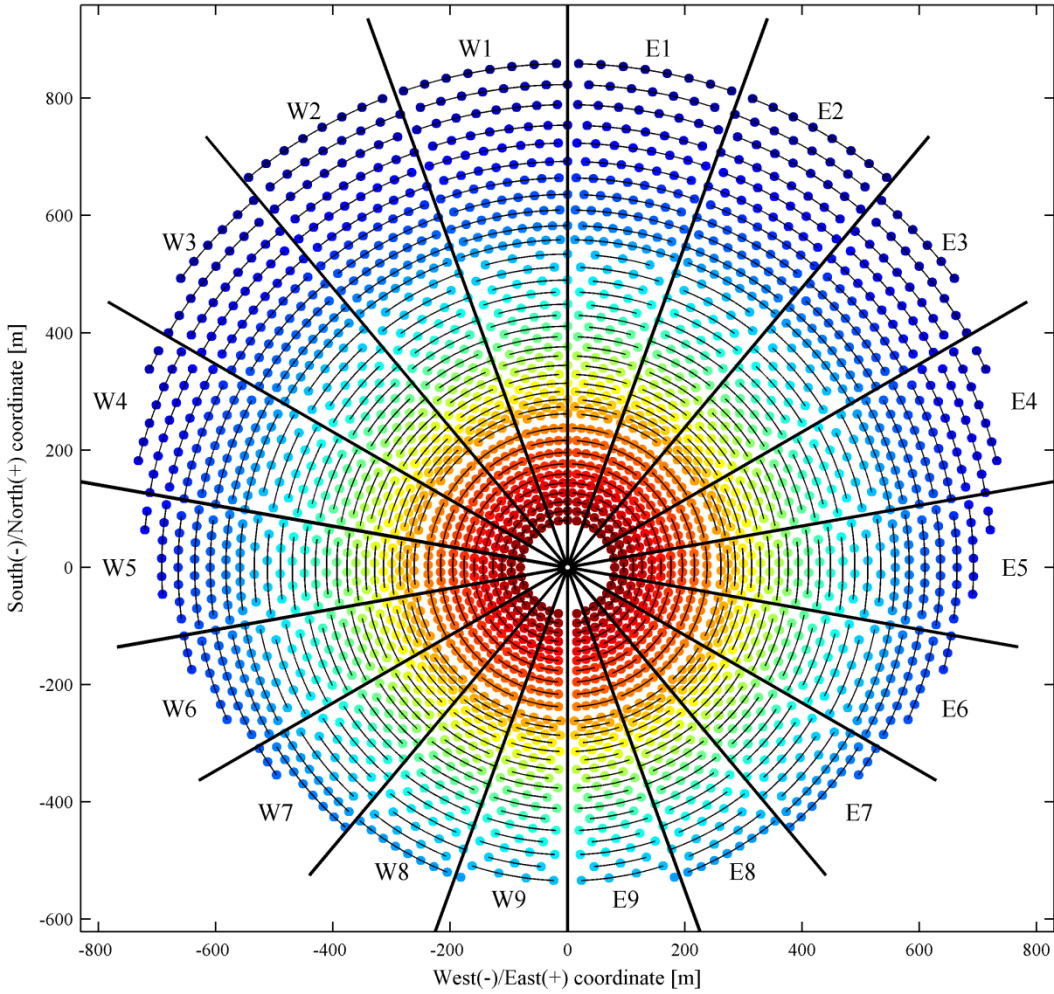
Fig. 3: Layout of Gemasolar heliostat field. Heliostats are colored by distance to the tower. Sectors are labeled corresponding to receiver panels and row-sector arc-lines are plotted.

The solar receiver is located at the top of a tower, whose optical height (*THT*) is 120 m. As shown in Fig. 4, the receiver comprises 18 panels (N_p) arranged around a cylindrical shell of 8.5 m diameter (*D*) and 10.5 m height (*H*). Outer diameter of tubes (d_o) is assumed to be 45 mm and its wall thickness (*th*), 1.5 mm; optimal tube parameters according to (Rodríguez-Sánchez et al., 2014b). Given 2 mm separation between tubes, each panel comprises 31 tubes within its 1.5 m width. Receiver tubes, which are made of Incoloy 800H, are coated with black Pyromark paint. Obviously, the computer code can handle input parameters other than those indicated for this case study.
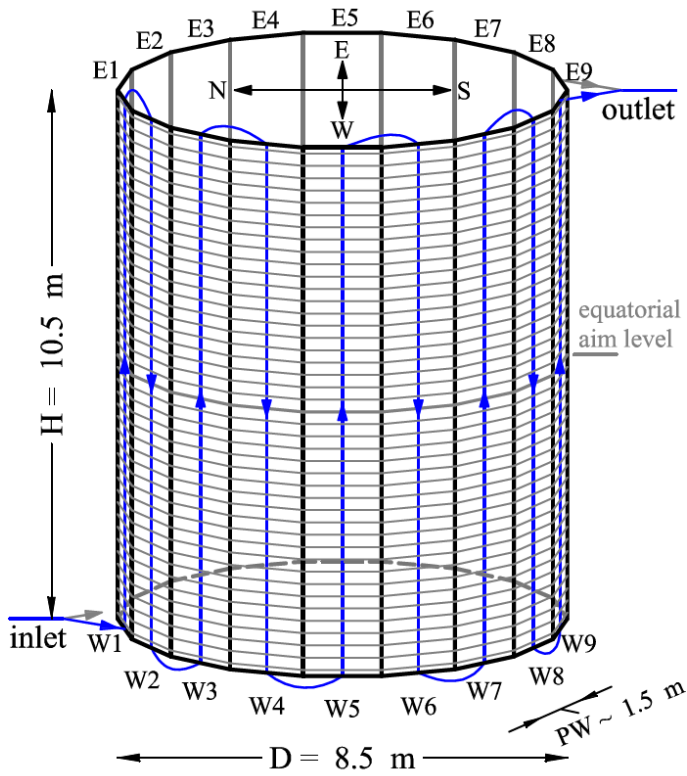
Fig. 4: Receiver geometry. East and west panels are numbered from inlet (north) to outlet (south); and west flow path is depicted. Gray horizontal lines designate the aim levels.

The HTF is molten nitrate salt, whose properties have been reported in (Zavoico, 2001). Under normal operation, salt inlet and outlet temperatures at the receiver are 290 and 565 ºC, respectively. The receiver inlet is at the north, where the flow is divided in two flow paths following a serpentine (up and down) flow pattern. Fig. 4 shows the west flow path in the receiver, where each panel is named according to both the flow path (east and west) and the panel number from inlet to outlet. No crossover has been considered as recommended in (Rodríguez-Sánchez et al., 2015).

4. Allowable flux density

Corrosion and thermal stress are the most critical issues in the operation of molten salt receivers. Both restrictions can be translated into maximum allowable flux densities (AFD) incident on the receiver, which is a parameter directly controllable by the aiming strategy. The ultimate allowable flux density is the minimum between corrosion (AFD_{corr}) and thermal stress (AFD_{strs}). In this section, a methodology to determine the allowable flux density in any receiver tube section is presented. Such methodology is illustrated for the case study plant at noon time of summer solstice (DNI=930, T_{amb}=35ºC).

4.1 Corrosion limit

Molten nitrate salts become corrosive at high temperature. The film temperature, defined as that at the inner surface of the tube, is the limiting factor. For Incoloy 800H the maximum film temperature $T_{f,lim}$ is 630ºC, according to (Bradshaw, 1987).

The corrosion temperature limit can be translated into a maximum flux density incident on the tube, i.e. an allowable flux density due to corrosion (AFD_{corr}). The receiver thermal model (Rodríguez-Sánchez et al., 2014b) is used to generate a database of AFD_{corr} depending on molten salt bulk temperature T_s and mass flow rate in the tube $\dot{m}_{s,t}$. The sequence of HTF mass flow rates hereafter used ranges from 0.6 to 5 kg/s in increments of 0.4 kg/s. By means of an iterative procedure, the flux density provoking a film temperature equal to the limit is found at each slice of a tube with a priori undefined length. The inlet and outlet temperatures of that virtual tube are 290 and 565ºC, respectively. The database generation procedure is indicated in Fig. 5.
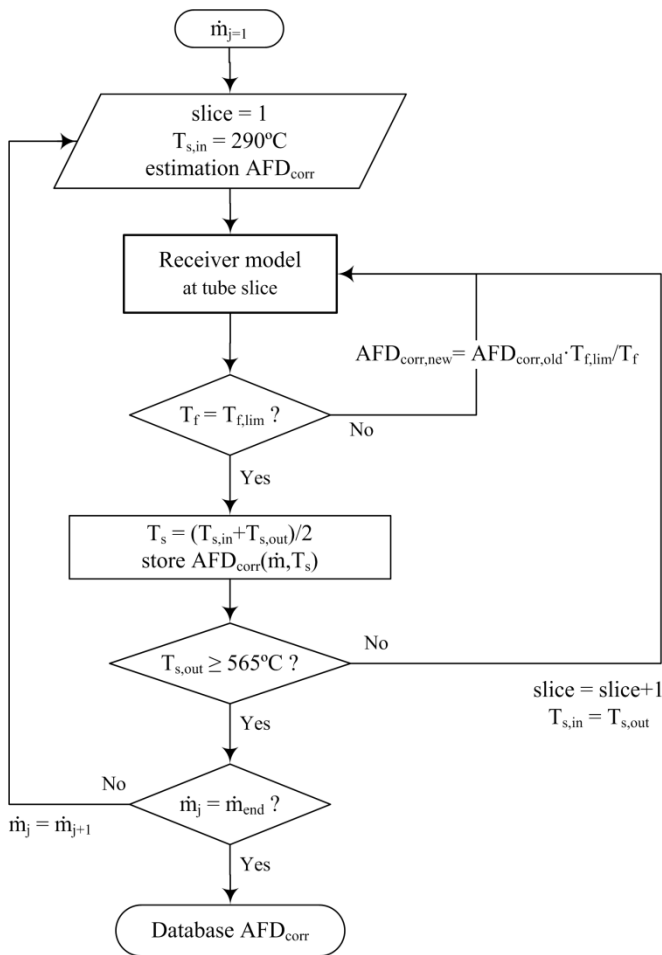

Fig. 5: Algorithm to generate the database of allowable flux densities due to corrosion.

Fig. 6 illustrates the resulting AFD_{corr} curves for Incoloy 800H. Clearly, the higher the mass flow rate, the higher the AFD_{corr} at a given salt temperature. The AFD_{corr} decreases when the molten salt bulk temperature increases; such decrement is more pronounced at higher mass flow rates.
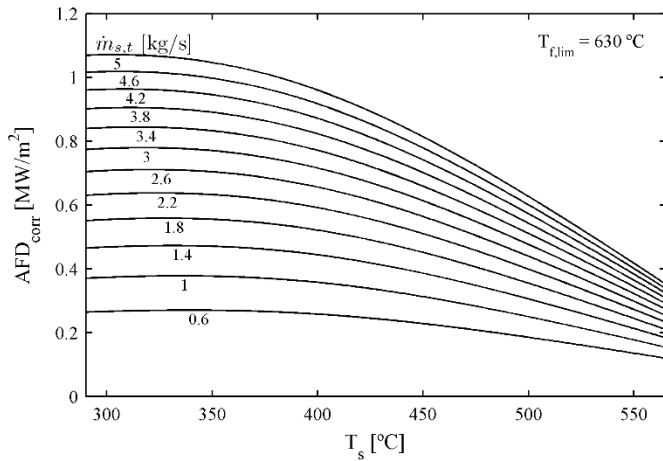
Fig. 6: Allowable flux density due to corrosion as a function of salt temperature and mass flow rate, given a maximum film temperature of 630ºC for alloy 800H. Valid for outer tube diameter 45 mm and wall thickness 1.5 mm.

Once the database of AFD_{corr} has been generated, it can be applied to any flux density distribution on the receiver in order to verify compliance with the corrosion limit. To determine the AFD_{corr} limit under a given flux map, the receiver model is run to find out both the molten salt mass flow rate and its temperature evolution along the receiver flow path. For the case study at summer solstice noon with single aiming, the mean flux density F profiles at each panel are shown in Fig. 7 (top), as well as the HTF temperature profile throughout the west flow path (bottom); east flow path is essentially symmetrical at noon. From the temperature profile and the mass flow rate, the AFD_{corr} red line is dictated. As can be checked in Fig. 7, film temperature at the intersections between F and AFD_{corr} is equal to 630ºC, which serves as verification of the calculation procedure for the AFD_{corr} database.
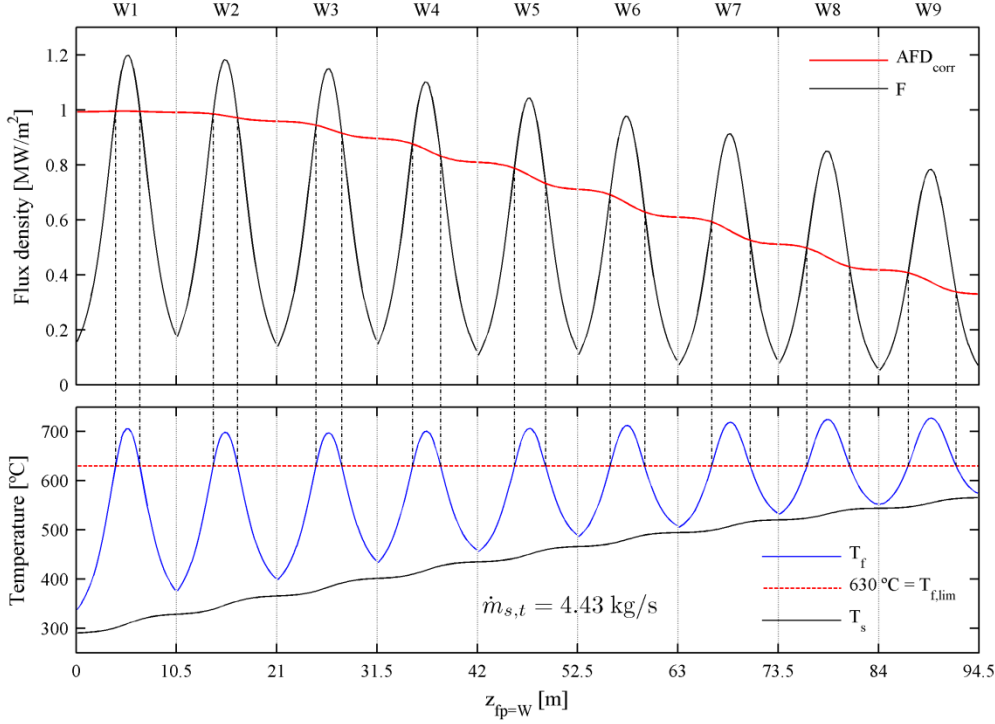
Fig. 7: Flux density (top) and salt and film temperature (bottom) throughout west flow path with equatorial aiming at summer solstice noon. Red lines designate allowable flux density due to corrosion and maximum film temperature.

4.2 Thermal stress limit

The main source of thermal stress in receiver tubes is the radial temperature gradient, because it is high in comparison with axial and circumferential temperature gradients, as (Irfan and Chapman, 2009) pointed out. Under a thermal gradient in the radial tube direction ΔT_r, longitudinal and tangential stresses S in the outer surface satisfy Eq. (4) (Young and Budynas, 2002). On the other hand, the conductive heat flux density at the outer tube surface q_o caused by a temperature difference in its thickness ΔT_r satisfies Eq. (5).

$$S_o = \frac{\Delta T_r \gamma E}{2(1-\nu)\ln(d_o/d_i)}\left(1 - \frac{2d_i^2}{d_o^2 - d_i^2}\ln\frac{d_o}{d_i}\right) \tag{4}$$

$$q_o = \frac{2 \cdot TC \cdot \Delta T_r}{d_o \cdot \ln(d_o/d_i)} \tag{5}$$

Combining Eqs. (4)-(5) (eliminating ΔT_r) and using the ultimate tensile strength *UTS* of the tube material for S_o, the maximum allowable heat flux density to the tube ($q_{o,lim}$) can be formulated as follows:

$$q_{o,\lim} = \frac{4 \cdot TC \cdot UTS(1-\nu)}{\gamma \cdot E \cdot d_o \left(1 - \frac{2d_i^2}{d_o^2 - d_i^2}\ln\frac{d_o}{d_i}\right)} \tag{6}$$

11

According to subsection NH of ASME Boiler and Pressure Vessel Code (ASME, 2004), long-time elevated temperature service reduces the tensile strength *TS* by a factor of one-third. For alloy 800H, Fig. 8 plots *TS* and the resulting *UTS* depending on the tube wall temperature, along with the rest of mechanical properties, taken from ASME Code. Substituting these values into Eq. (6), the maximum heat flux density to the tube $q_{o,lim}$ is determined as a function of the outer surface temperature; which is represented by the dashed line in Fig. 9.
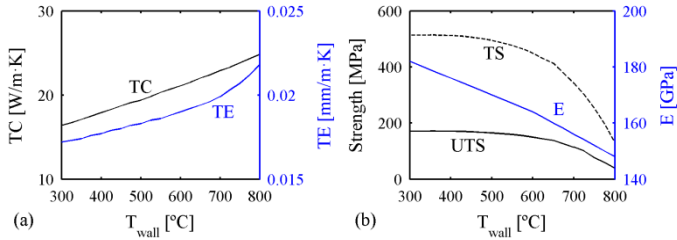

Fig. 8: Mechanical properties of alloy 800H as a function of wall temperature: (a) thermal conductivity and thermal expansion; and (b) tensile strength, ultimate tensile strength and Young's modulus.

Because the maximum tube temperature takes place at the crown, radiation losses are to the surroundings, and the calculation is straightforward by means of Stefan-Boltzmann law. Convection losses are again estimated in accordance with (Siebers and Kraabel, 1984). The flux density limit ($F_{lim,strs}$) incident on the receiver results from adding radiation and convection losses to the maximum heat flux to the tube $q_{o,lim}$. The solid line in Fig. 9 represents such flux density limit.
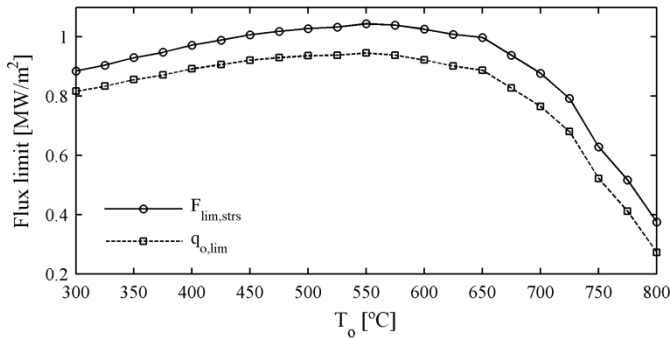

Fig. 9: Maximum flux density incident on ($F_{lim,strs}$) and absorbed by ($q_{o,lim}$) the tubes due to thermal stress, depending on the outer temperature of the tube.

Allowable flux densities due to thermal stress (AFD_{strs}) are found in the intersection between the profile of incident flux density *F* and the above described $F_{lim,strs}$. For the case study at summer noon, both profiles are shown in Fig. 10 (top) when equatorial aiming is set. The blue $F_{lim,strs}$ curve derives from the crown temperature T_o profile shown below, which is an output of the receiver model. Several flux maps (i.e. aiming strategies) should be needed in order to determine enough points of the AFD_{strs}, however it has been proved that intersection points for different *F* profiles have almost constant vertical coordinate in each panel; i.e. the AFD_{strs} is almost uniform. Therefore, the AFD_{strs} has been set constant and equal to that found in the intersection

12

between $F_{lim,strs}$ and F with single aiming. The horizontal magenta segments in Fig. 10 indicate the AFD_{strs} at each panel.
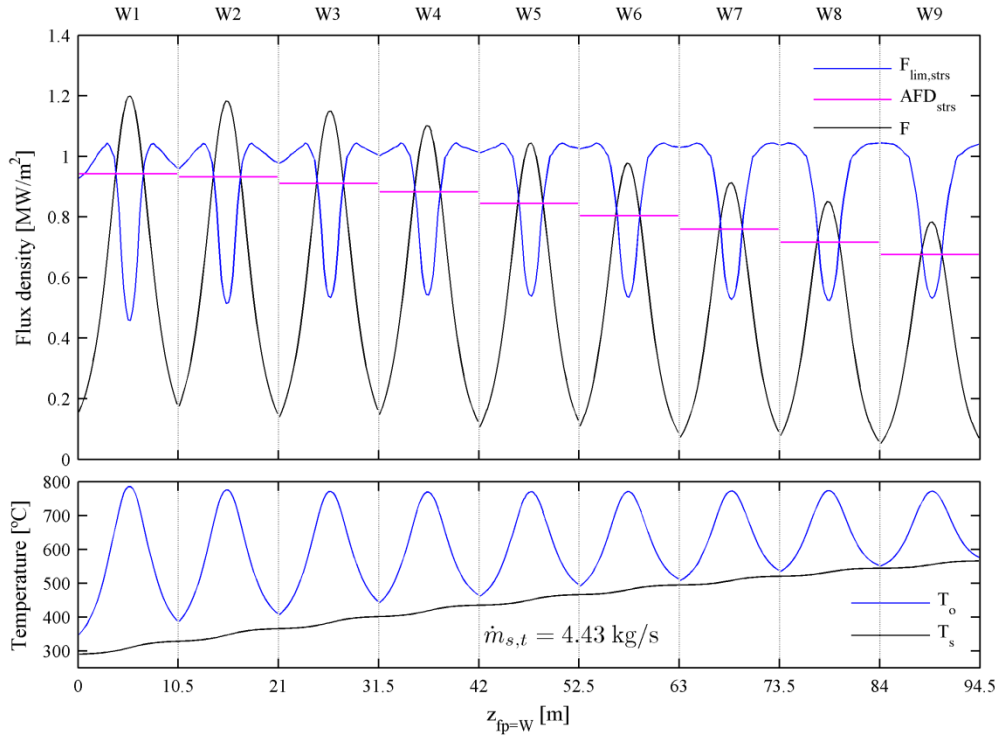

Fig. 10: Flux density (top) and salt and outer wall temperature (bottom) throughout west flow path with equatorial aiming at summer solstice noon. Horizontal magenta lines designate the allowable flux density due to thermal stress at each panel, obtained through the intersection between actual flux density and stress limit.

5.   Algorithms

The objective of the aiming strategy model is to automatically aim heliostats in a way that attempts to collect as much as possible solar flux on the receiver. This is equivalent to reduce spillage losses, which in turn protects the oven covers from overheating. At the same time, the flux distribution must not exceed the allowable flux density limits due to corrosion and thermal stress, presented in the previous section.

An odd number of horizontal target lines is established, since heliostats can be vertically aimed at discrete points in cylindrical receivers. For instance, these aim levels can coincide with the receiver mesh, as herein used. Given a nodal spacing of about 25 cm, it results in the 43 vertical aim levels depicted in Fig. 4. Treated as a classical combinatorial problem, the total amount of possible aiming combinations equals 43^{2650}, for the heliostat field in the case study consisting in 2650 heliostats.

In the present study, the heliostats in each row-sector are aimed at the same height level. Such row-sectors are plotted with arc-lines in layout Fig. 3, where each field sector is labeled in correspondence with its target panel. From 602 row-sectors, 43^{602} aiming combinations are still feasible. Evaluating each possible combination (i.e. exhaustive search) is intractable in terms of computation time. A fast algorithm to reach the main goal is also

13

another objective. These purposes are accomplished by means of the two algorithms –search and fit– described in this section.

5.1 Search algorithm

The purpose of the search algorithm is to find the higher aiming factor for each field sector (k^{sector}) with which the *AFD* limit could be met on the basis of a symmetric aiming strategy with respect to the equatorial line. As formerly introduced in (Vant-Hull, 2002), heliostats can be aimed in such a way that the beam circumference is tangent to either the upper or the lower receiver edge. Given a *k* factor, Eq. (2) estimates the beam radius BR_k for any heliostat, as shown in Fig. 11a, and the target point is located at the aim level whose distance to the rim is nearest, being equal or greater than BR_k. Because of the influence of *k* value on the target position, it was named *aiming factor*. Besides, *k* provides a measure of the spillage loss; the lower *k* factor is, the lower interception is achieved.
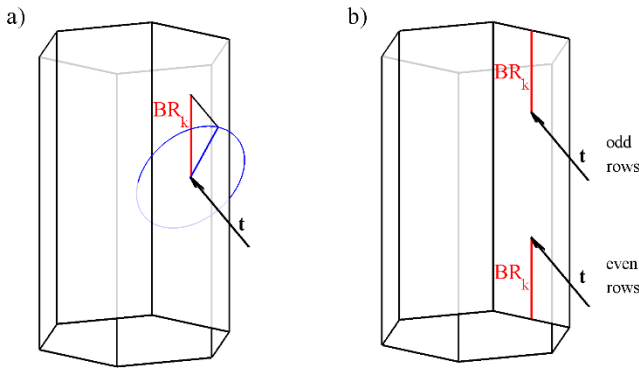

Fig. 11: Symmetric aiming strategy: a) estimation of beam radius based on k factor, and b) target positioning.

Azimuth angle of the aim point is kept equal to that of the heliostat, therefore only vertical shift is considered. In this instance, heliostats in even rows are aimed at the bottom and odd rows at the top, as shown in Fig. 11b. Evidently, heliostats whose beam diameter is greater than the receiver height (i.e. $BR_k > H/2$) are aimed at the equator. This aiming strategy leads to practically symmetric flux maps with respect to the equator (i.e. receiver mid-plane), as previously shown in (Sánchez-González and Santana, 2015).

The search algorithm is divided into two sequential parts named: sweep and adjustment routines, described in the following.

5.1.1   Sweep routine

As the name suggests, this algorithm performs a sweep of aiming factors starting from a high *k* value (i.e. low spillage). The purpose is to find for each field sector the first (highest) aiming factor that does not exceed the allowable flux density limit. The *AFD* profile limit throughout each flow path is kept fixed, even though this profile changes with the aiming. This way a preliminary *k* factor is quickly found for each field sector.

The sequence of k aiming factors swept in this algorithm is defined on the basis of the aim levels. A high number of k factors would result in heliostats aiming at the same height level, along with a large computation time. On the contrary, a small number of k factors would result in low accuracy. It has been proved that a number of aiming factors equal to half the aim levels provides a favorable sweep resolution when the k values are logarithmically spaced; note that the cumulative energy within half of a beam as a function of its radius follows a rather logarithmic distribution. Starting from $k=3$, which is almost equivalent to equatorial aiming, and until $k=0.2$ (heliostats aiming at the receiver edge would mean $k=0$), the sequence of 22 aiming factors used in the case study is: $k_j = [3\ 2.64\ 2.32\ 2.04\ 1.79\ 1.57\ 1.38\ 1.22\ 1.07\ 0.94\ 0.83\ 0.73\ 0.64\ 0.56\ 0.49\ 0.43\ 0.38\ 0.34\ 0.29\ 0.26\ 0.23\ 0.2]$.

Fig. 12 depicts the detailed flowchart of the sweep routine. The receiver model is run only once in order to establish the AFD profile limit, which corresponds to the higher aiming factor (i.e. $k=3$). Using the symmetrical aiming strategy the whole flux map is assembled for each aiming factor following the sequence stated above. If the flux profile is under the AFD limit for any receiver panel, such k factor is stored for the corresponding field sector. This acceptance criterion is formulated as $F_{k,p} < AFD_p$. The calculation procedure stops when k values are assigned to every field sector, avoiding the computation of unnecessary cases.

Because a symmetric aiming strategy with respect to the equator is used at this stage, it is known that two shoulders emerge in the flux density profile when the aiming factor is low enough. In some cases, aim points could be redistributed to balance the energy flux surpassing the AFD limit. Finding the outermost intersection point between F and AFD, and defining a vertical range between that point and its symmetrical about the middle point in the panel, the difference between F and AFD profiles is computed within that range. From the graphical interpretation shown in detail 2 within Fig. 13, if the area of the region over the AFD limit (A_{over}) is smaller than the area of the region under (A_{under}), the balance is presumed. Hence, the alternative acceptance criterion is defined as $A_{over} < A_{under}$, as stated in flow chart Fig. 12.
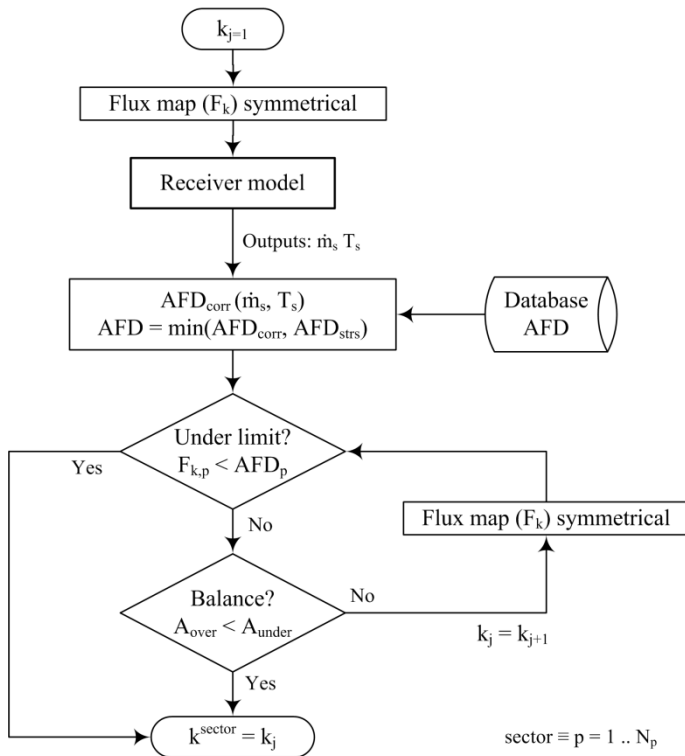
Fig. 12: Flowchart of the sweep routine.

For the case study at summer noon, Fig. 13 represents the profiles of flux density along the sweep calculation throughout the west flow path. For the 22 aiming factors defined above, the corresponding F profiles are depicted in the figure. The allowable flux density is represented for both the corrosion and the thermal stress limits, although the actual AFD limit (plotted as solid line) is the lower of the two. In the following figures, only the actual AFD will be displayed.

The selected F profile at each panel is indicated by blue thick line and its corresponding sector aiming factor k^{sector} is displayed at the bottom. The under limit criterion is met in the first five panels, whereas for panels 6 to 9 the balance is achieved. A caption of the flux density profiles in the last panel is shown in Detail 1 (Fig. 13). F profiles corresponding to the last nine aiming factors are also represented, even though their computation is unnecessary.
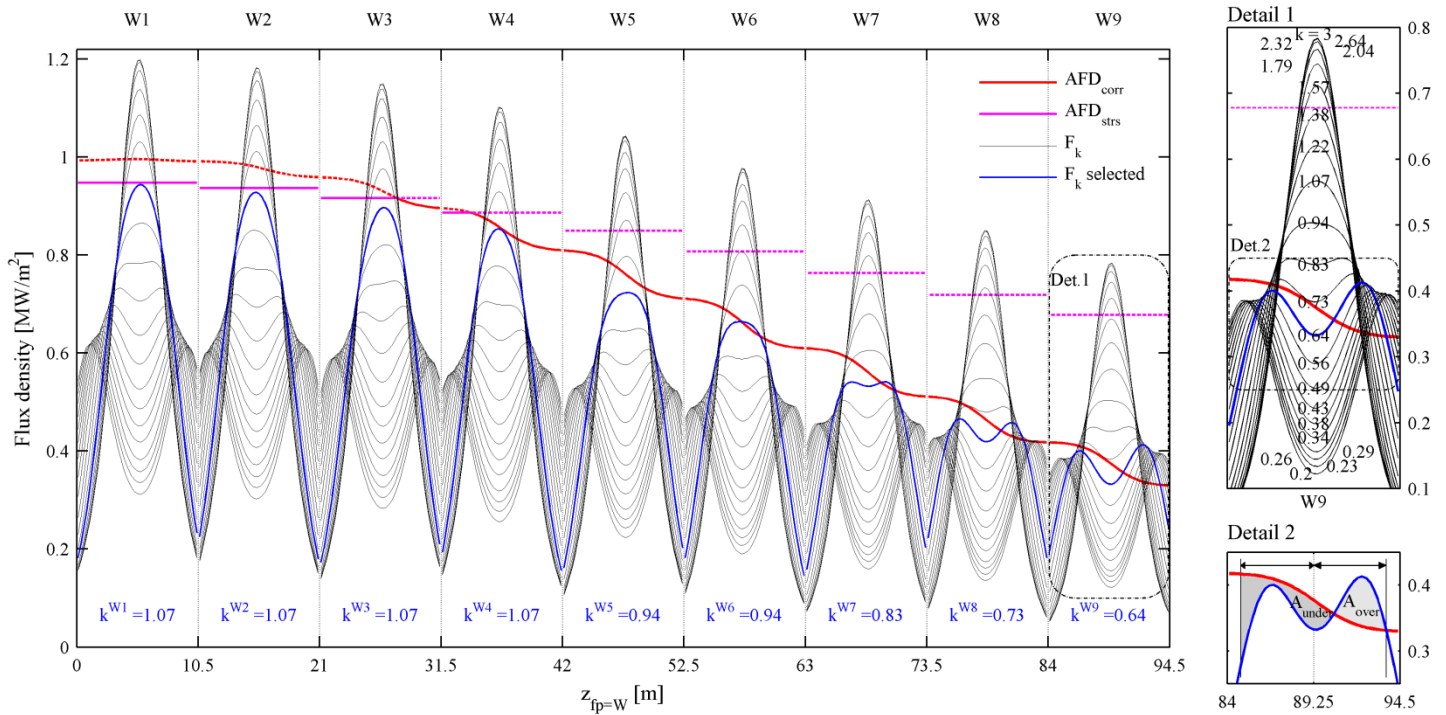
16

Fig. 13: Profiles of flux density, throughout west flow path at summer solstice noon, generated for different aiming factors (sweep). Selected profile at each panel and its corresponding aiming factor are colored in blue. On the right, detail 1 enlarges the sweep on the last panel and detail 2 stands for the balance between flux over and under the limit. Allowable flux densities due to corrosion and thermal stress are colored in red and magenta, respectively; the most restrictive limit is plotted as solid line.

5.1.2 Adjustment routine

In general, a modification of the aim points changes the molten salt mass flow rate and its temperature evolution through the flow path, because of the outlet set point temperature (565 ºC). Consequently, the AFD_{corr} limit is modified. In the preceding sweep routine the AFD corresponded to that for the higher aiming factor (k=3). The adjustment routine precisely adjusts the preliminary aiming factors from the sweep routine taking into account the real AFD limit.

The adjustment routine (Fig. 14) checks the same acceptance criteria than the sweep routine, but updating the AFD using the receiver model and the AFD database. Besides, the aiming factor is only increased in those sectors in which neither the under limit criterion nor the balance are met.
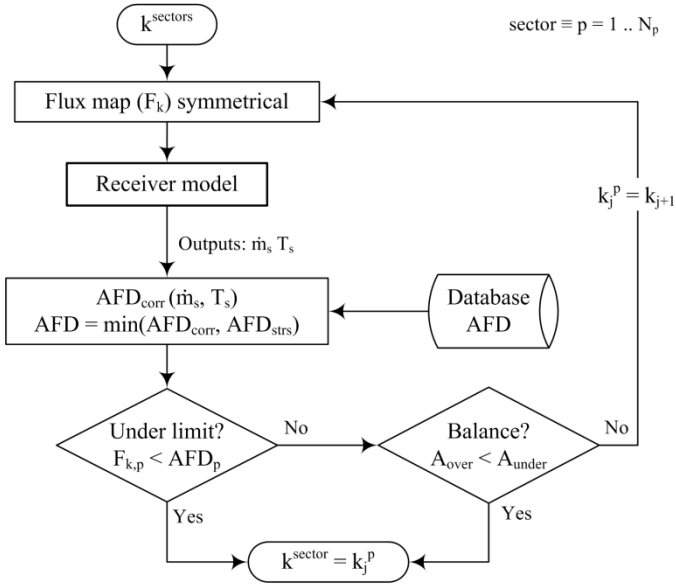
17

Fig. 14: Flowchart of the adjustment routine.

Fig. 15a (top) shows the actual *AFD* limit along with the *F* profile for the aiming factors obtained from the sweep routine. However the acceptance criteria is not met in the last two panels, since the *AFD* has been lowered; $\dot{m}_{s,t}$ has changed from 4.43 to 4.27 kg/s.
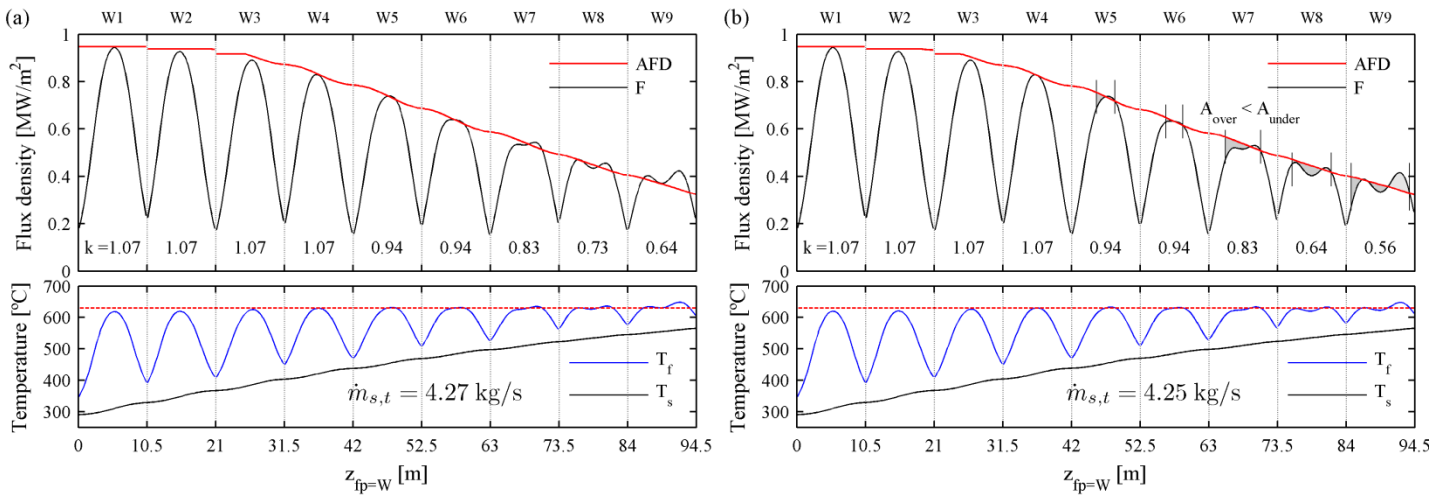

Fig. 15: Flux density (top) and salt and film temperature (bottom) throughout west flow path at summer solstice noon for: (a) aiming factors resulting from the sweep routine, and (b) aiming factors after performing the adjustment routine.

After the adjustment routine is applied, the aiming factor in the last two sectors decreases, until the *AFD* limit recomputed in each iteration is achieved. As a consequence, interception slightly decreases, likewise mass flow rate. Now the under limit criterion is met in panels 1 to 4 and the balance is achieved in the last 5 panels.

5.2 Fit algorithm

In the previous search algorithm a symmetrical aiming strategy was utilized to quickly find preliminary aiming factors at each field sector $k^{sectors}$. The flux density vertical profile in each panel is consequently symmetric respect to the equator, as opposed to the AFD profile which decreases along the flow path.

The purpose of the fit algorithm (Fig. 16) is to select the heliostat target points such that the flux F profile properly fits the AFD limit. The range of aim levels that can be targeted for each row-sector is established from the $k^{sectors}$ obtained in the search algorithm. Among the possible aiming points, the fit algorithm selects that one which maximizes the difference between F and AFD. In other words, the fit algorithm deals with accommodating the flux profiles for each row-sector in such a way that the subtraction $AFD–F$ is the maximum possible.

The order in the superposition of the flux maps produced by each heliostat is a key factor to the success of the algorithm. Since the flux reflected by a heliostat impacts into not only the panel corresponding to its field sector, but also the nearby panels, the possible images by a whole row of heliostats must be added together, although the accommodation is performed row-sector by row-sector. It is favorable to sort the rows depending on the number of feasible aim levels, seen as degrees of freedom. Accordingly, rows are sorted from higher to lower beam radius (r^{sort}).

Fig. 16 represents the detailed flowchart of the fit algorithm, where the acceptance criterion is restricted to not surpassing the AFD limit. In case of rejection, the aiming factor is lowered to the next in the k_j list. At the end, the receiver model is run and the AFD updated to check whether this limit remains undisrupted.

Data from search algorithm

Beam size of row-sectors from $k^{sectors}$
Rows sorted from higher to lower beam size (r^{sort})
Initialization: $F_{ap} = 0$

$r^{sort}_{j=1}$

Possible aiming points (ap)

Flux map of row-sectors $F_{r,p,ap}$
$F_{ap} = F_{ap} + F_{r,p,ap}$

Accomodate:
select aiming point (ap) such that ($AFD - F_{ap}$) is maximum

$r^{sort}_j = r^{sort}_{end}$?

No → $r^{sort}_j = r^{sort}_{j+1}$

Yes

Under limit?
$F_p < AFD_p$

No → $k_j^p = k_{j+1}$

Yes

Receiver model

Outputs: $\dot{m}_s$ T_s

$AFD_{corr}(\dot{m}_s, T_s)$
$AFD = \min(AFD_{corr}, AFD_{strs})$

Database AFD

Under limit?
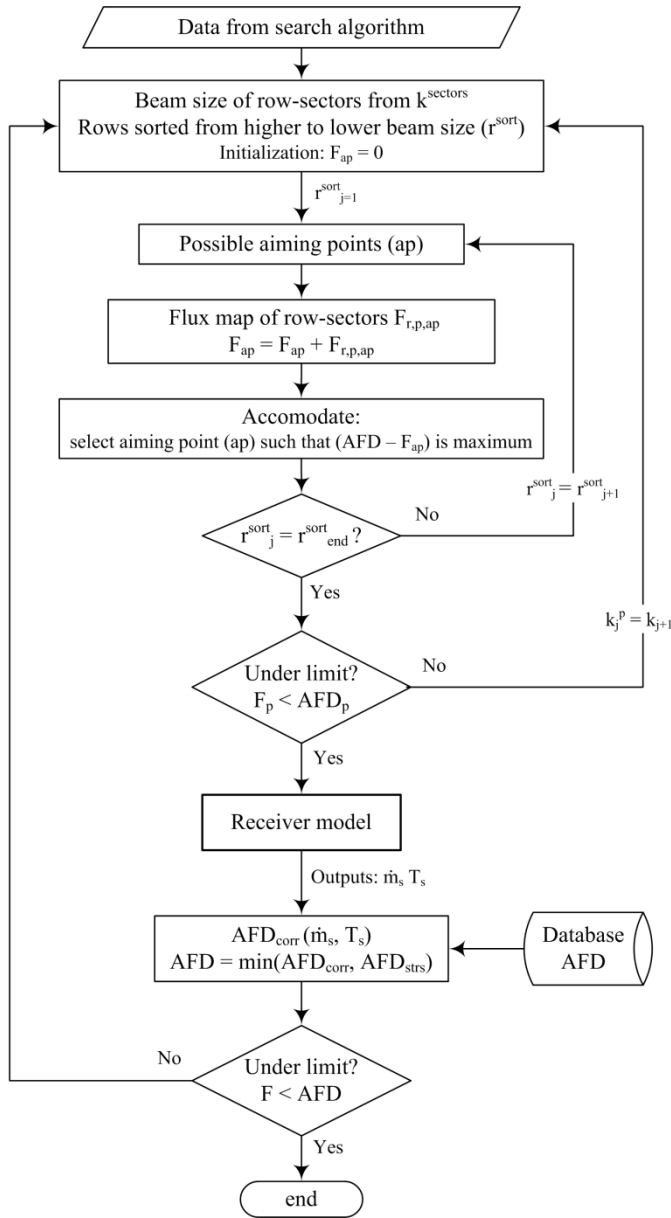$F < AFD$

No

Yes

end

Fig. 16: Flowchart of the fit algorithm.

For the case study presented in this study, Fig. 17 represents the profile of flux density in the west flow path resulting from the fit algorithm. The cumulative *F* profiles after each row addition are colored according to the code in Fig. 3. The last curve corresponds to the final flux density profile that never surpasses the *AFD* boundary. The *F* profile tends to match the *AFD* limit in the central region of the panel.

At the bottom of Fig. 17, it is checked that the film temperature profile does not surpass the 630ºC corrosion limiting temperature. To keep the outlet salt at 565 ºC, the mass flow rate of molten salt in the tubes has been slightly reduced with respect to that before the fit algorithm. Therefore the thermal power has been marginally decreased, which entails that the spillage has been also slightly increased.
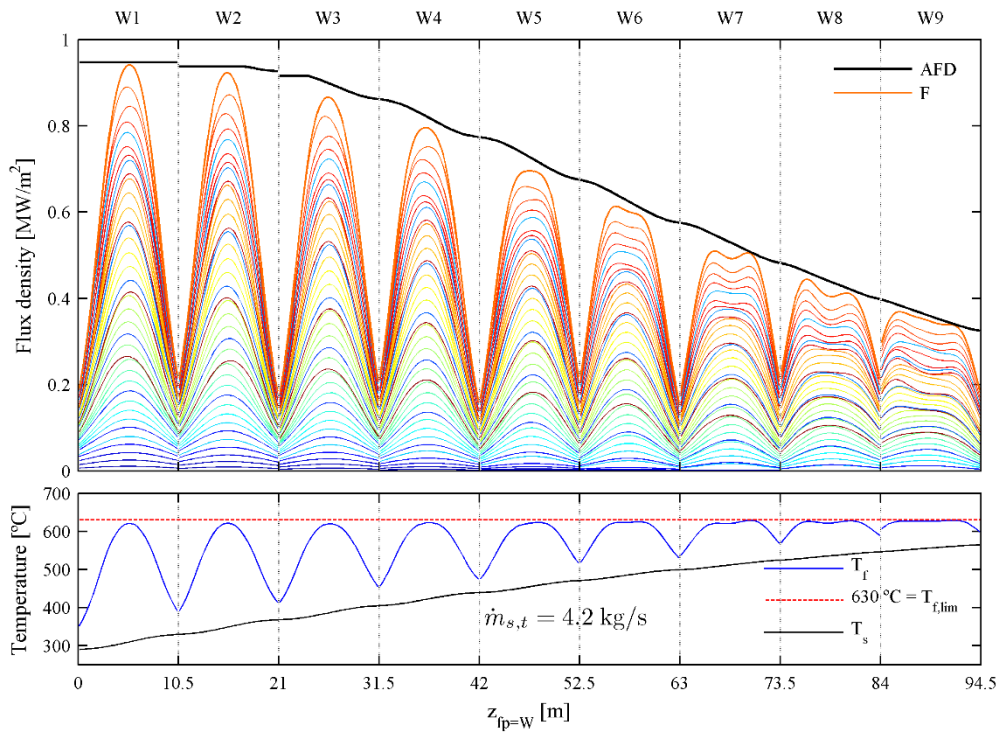
Fig. 17: Profiles of flux density (top) and salt and film temperature (bottom) throughout west flow path at summer solstice noon. Each heliostat row image is added during the fitting process in the order denoted by the color that corresponds to those in Fig. 3.

A single node on an Intel Core i5-2400 microprocessor (3.1 GHz) with 4 GB memory was used to perform the simulation. For the case study, the fit algorithm required on average 54.4 s of CPU time, and the search algorithm (sweep plus adjustment), 72.3 s.

6.   Results and discussion

In this section we present and discuss the outputs from the proposed aiming strategy model. Using the Gemasolar-like case study presented in section 3, the results at different solar times of the summer solstice are examined. Along with the profiles of flux density and temperatures throughout the two flow paths, the heliostat aim points and the resulting flux maps are reported.

For the noon time case used to illustrate the algorithms in the preceding section, the profiles of flux density and temperature –bulk and film– are represented in Fig. 18 for east (left) and west (right) flow path. As expected, results for both flow paths are noticeably symmetrical; negligible difference exists between both mass flow rates.
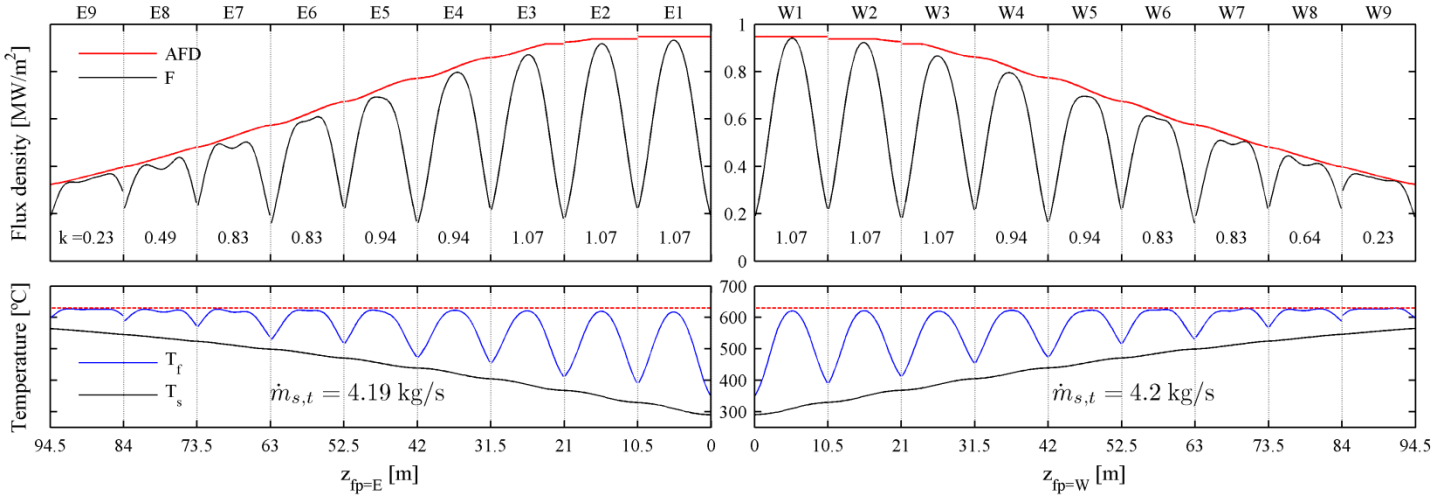
Fig. 18: Flux density (top) and salt and film temperature (bottom) throughout east (left) and west (right) flow path at summer solstice noon (*DNI* = 930 W/m^2).

The aiming point of each heliostat in the field is marked in Fig. 19, where the 3D surface of the receiver is unfolded. The heliostat corresponding to each aim point can be identified with the aid of Fig. 3, attending to the color of the row and the heliostat sector or azimuth. At the same time, the distribution of flux densities on the receiver is plotted in the background. This grayscale flux map complements the mean *F* profiles shown in previous Fig. 18.

Paying attention to the aim points, these are located in the equatorial belt or evenly spread around it for the first two panels in both circuits. In the rest of the panels, target points tend to distribute unequally. Heliostats far from the receiver aim to the equator, whereas near heliostats' aim points are shifted to the panel entrance; top for downstream and bottom for upstream panels. Roughly speaking, the closer the heliostat is to the receiver, the farther the aim point from the middle is.
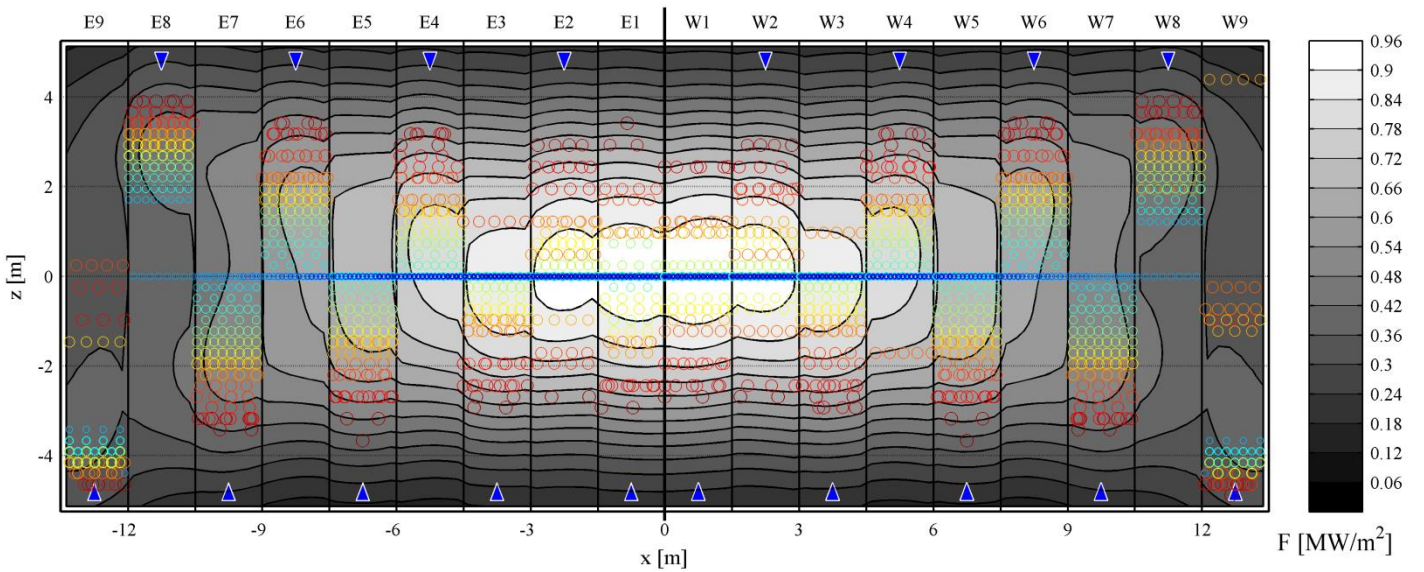
Fig. 19: Flux density distribution at summer solstice noon ($DNI = 930$ W/m^2). Circles represent the aim point of each heliostat colored by its distance to the receiver, according to Fig. 3. Triangles point out the direction of the flow at each receiver panel.

At solar times other than noon, outputs are different for east and west flow path. Before noon higher radiation is received from the west side of the heliostat field, and vice versa. At 9:00, receiver west flow path captures 30% more thermal energy than east side, as can be inferred from the mass flow rates displayed on Fig. 20. Just because of higher $\dot{m}$ in the west circuit, its AFD_{corr} limit is also higher compared to the east for the same z_{fp} distance.

Flux profiles perfectly fit the AFD limit in the central region of each panel, except for panels 7 and 8 in west side where valleys are formed. It must be pointed out that adjacent panels demand opposed flux patterns since the flow path is serpentine-like and the higher AFD is usually located at the entrance of each panel. Meeting contrary requirements is occasionally unattainable, as occurs for panels 7 and 8. The last panel of both flow paths is less affected by this issue due to their coincident flow direction.
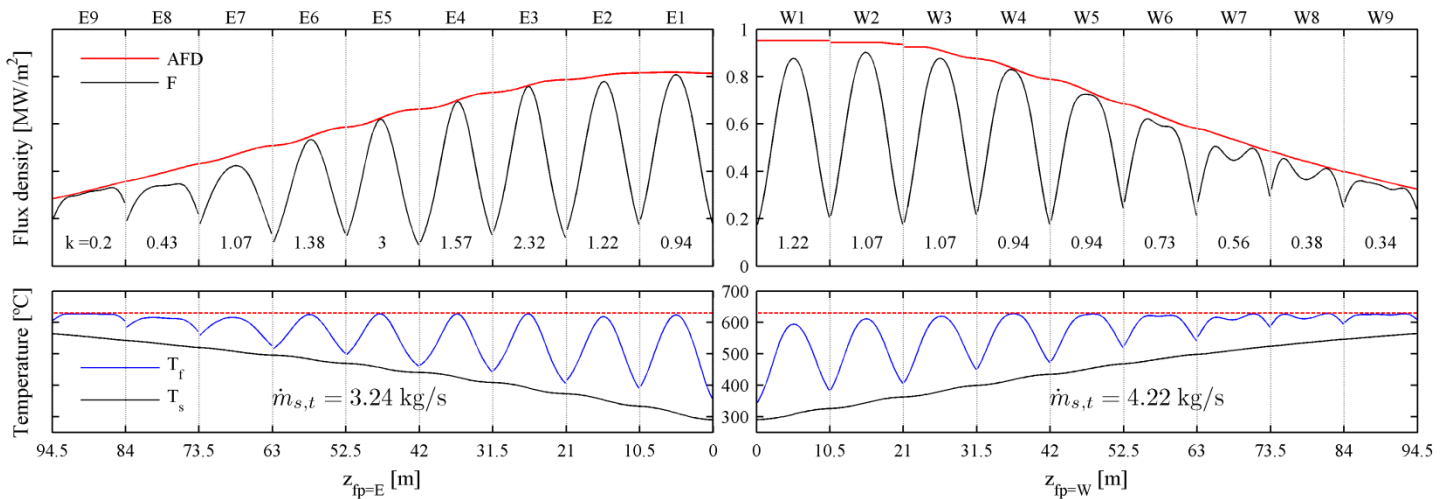

Fig. 20: Flux density (top) and salt and film temperature (bottom) throughout east (left) and west (right) flow path at 9 solar time at summer solstice ($DNI = 910$ W/m^2).

Aiming factors, displayed in Fig. 20, in the west side are regularly smaller than in the east. Consequently, greater vertical shifting of aim points is found in the west, see Fig. 21. As expected, the peak flux density (0.91 MW/m^2) is detected at the anti-sun location.
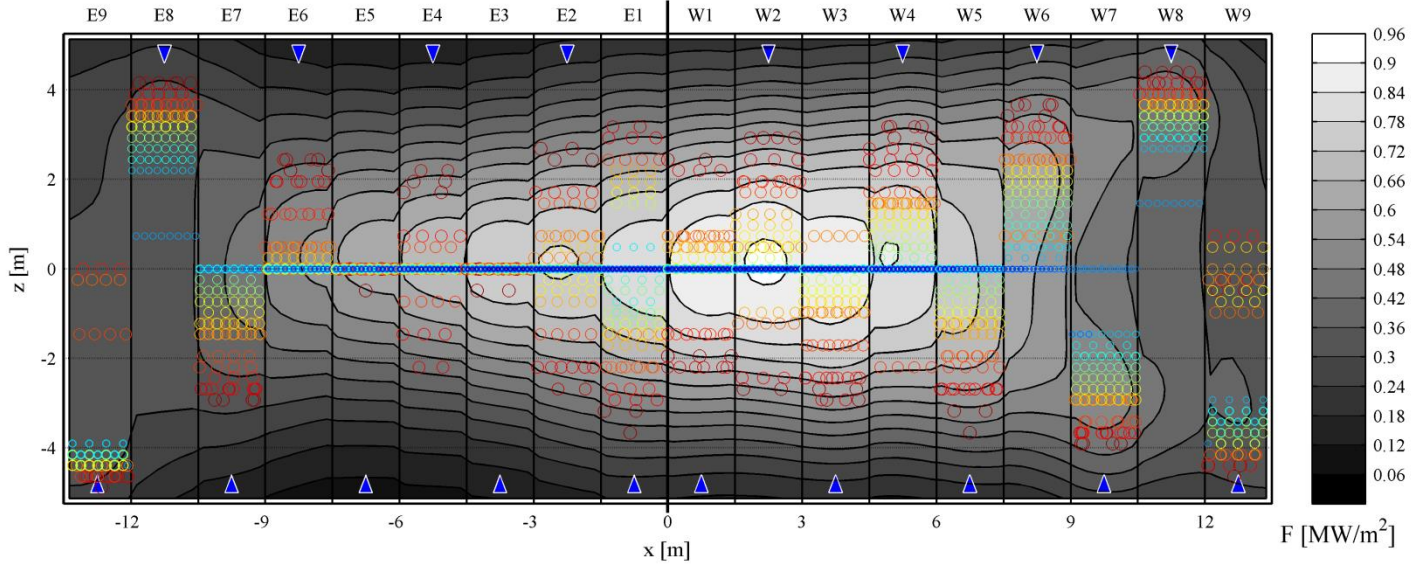
Fig. 21: Flux density distribution at 9 solar time at summer solstice (*DNI* = 910 W/m²). Circles represent the aim point of each heliostat colored by its distance to the receiver, according to Fig. 3. Triangles point out the direction of the flow at each receiver panel.

Earlier in the morning, at 7:00, solar radiation incident on the receiver is lower, since direct normal irradiance (770W/m²) is reduced, as well as the optical field efficiency mostly due to cosine and shading losses. As a consequence, the thermal power output from the receiver diminishes, as can be deduced from the mass flow rates displayed in Fig. 22.
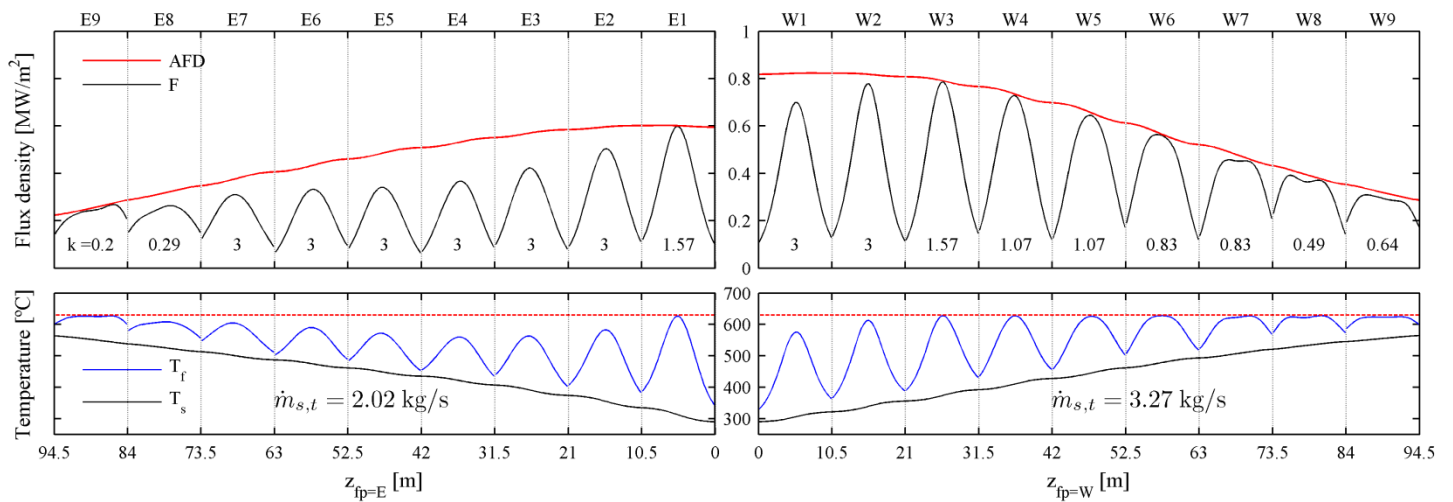

Fig. 22: Flux density (top) and salt and film temperature (bottom) throughout east (left) and west (right) flow path at 7 solar time at summer solstice (*DNI* = 770 W/m²).

The *AFD* is not reached in most of the east side panels, even aiming at the equator. On the contrary, to match the boundary in the west side, heliostats have to aim at different levels, as can be seen in Fig. 23. Regardless of solar time, the last panels of both flow paths always require considerable vertical aim shifting which results in significant spillage loss.
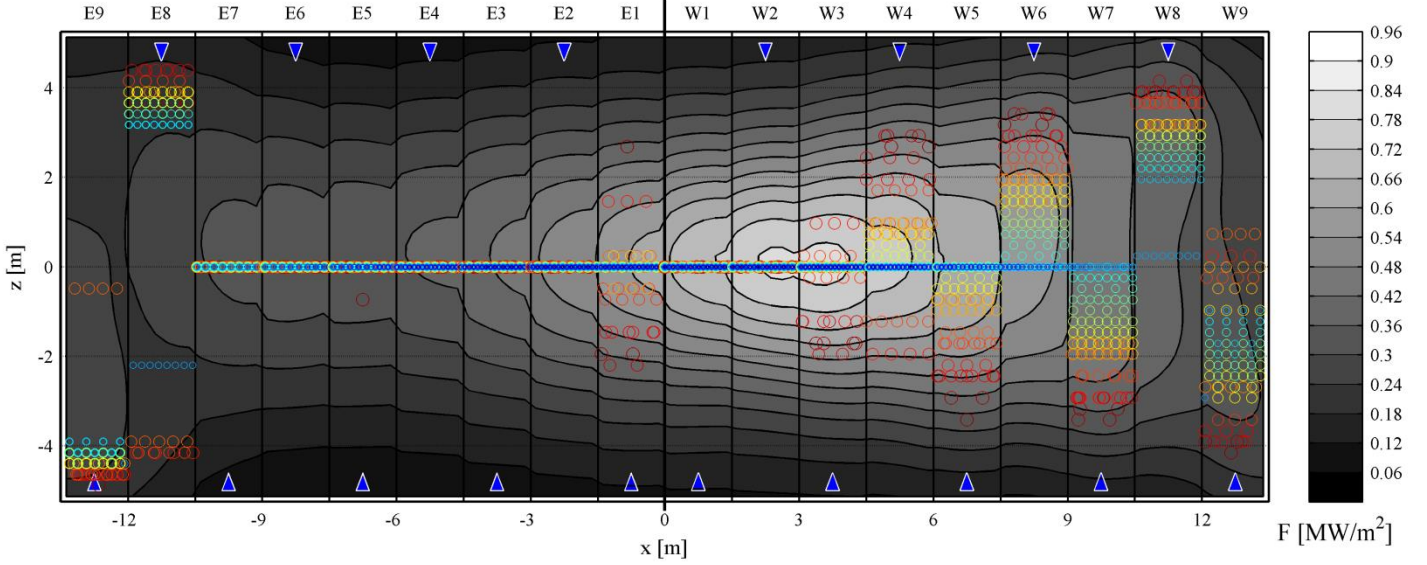
Fig. 23: Flux density distribution at 7 solar time at summer solstice (*DNI* = 770 W/m²). Circles represent the aim point of each heliostat colored by its distance to the receiver, according to Fig. 3. Triangles point out the direction of the flow at each receiver panel.

The corrosion limiting film temperature of 630ºC is nowhere exceeded, as seen in previous figures, which confirms the validity of the model. For different solar times at summer solstice, the maximum film temperature $T_{f,max}$ along with other key outputs are summarized in Table 1, which compares the model with the equatorial aiming. To meet the corrosion and thermal stress limits, the peak flux density becomes drastically reduced in the achieved aiming up to 23%. Nonetheless, the interception factor f_{int} falls no more than 0.04 points, because of the vertical spreading of aim points. The model ensures that the minimum possible spillage losses are added and the receiver output is thus maximized. Compared to the unfeasible single aiming, the receiver thermal power Q_{rec} is slightly reduced up to 6%.

Table 1: Equatorial versus optimized aiming strategy. Output parameters for summer solstice.

Solar time	DNI [W/m2]	$T_{f,max}$ [ºC]		F_{max} [MW/m²]		f_{int}		Q_{rec} [MW]	
		Eq.	Opt.	Eq.	Opt.	Eq.	Opt.	Eq.	Opt.
12	930	727	629	1.208	0.948	0.819	0.786	114.7	108.7
11	930	731	629	1.210	0.934	0.818	0.783	113.7	107.4
10	920	734	629	1.188	0.928	0.817	0.780	109.2	103.0
9	910	736	629	1.157	0.910	0.813	0.777	102.7	96.7
8	860	733	630	1.060	0.902	0.809	0.774	90.3	85.2
7	770	725	628	0.880	0.795	0.802	0.774	71.7	68.4
6	600	699	628	0.533	0.526	0.793	0.777	42.3	41.2

7.   Conclusions

We have presented a model to determine a nearly optimal aiming in CRS. The model consists of two iterative algorithms that search the aim points for the heliostats in a field. The objective is to attempt to maximize the interception and hence the receiver thermal power output, while preserving the integrity of the receiver. For the Gemasolar-like case study presented in this paper, the spillage factor falls just 0.04 points compared to the unreliable equatorial aiming.

The two major constraints in molten salt receivers –corrosion and thermal stress– have been translated into allowable flux densities. The model uses these *AFD* limits within which heliostat flux densities are favorably accommodated. Besides the main algorithms, we have successfully developed a calculation procedure to generate a database of *AFD* due to corrosion. The model also computes the thermal stress limits that can be predominant in the first receiver panels, where a rather flat flux profile is preferred in the central region.

It has been found that, for most of the panels, the expected flux density profile has its peak displaced to the entrance of each receiver panel. This favorable flux profile has a slope towards the panel outlet that is more pronounced in the middle panels; those oriented to east and west. Serpentine flow pattern in cylindrical multi-panel receivers entails contrary requirements for adjacent panels, since the peak flux is expected at opposite heights. Despite this conflicting demand, the fit algorithm is capable of substantially matching the *AFD* profile.

The resulting tool is capable of accurately determining the optimal aim points for the heliostats in any field at any time. Because of its automatic and fast computation (around 2 minutes in a single core standard CPU), this aiming tool can be applied to the open-loop control and real-time operation of heliostat fields. Furthermore, an integrated design of heliostat field and central receiver is feasible on the basis of the developed aiming model.

References

ASME, 2004. ASME Boiler and Pressure Vessel Code. American Society of Mechanical Engineers, New York.

Belhomme, B., Pitz-Paal, R., Schwarzbözl, P., 2013. Optimization of Heliostat Aim Point Selection for Central Receiver Systems Based on the Ant Colony Optimization Metaheuristic. J. Sol. Energy Eng. 136, 011005.

Besarati, S.M., Yogi Goswami, D., Stefanakos, E.K., 2014. Optimal heliostat aiming strategy for uniform distribution of heat flux on the receiver of a solar power tower plant. Energy Convers. Manag. 84, 234–243.

Bradshaw, R.W., 1987. Thermal Convection Loop Study of the Corrosion of Incoloy 800 in Molten NaNO3-KNO3. Corrosion 43, 173–178.

Collado, F.J., Gómez, A., Turégano, J.A., 1986. An analytic function for the flux density due to sunlight reflected from a heliostat. Sol. Energy 37, 215–234.

García-Martín, F.J., Berenguel, M., Valverde, A., Camacho, E.F., 1999. Heuristic knowledge-based heliostat field control for the optimization of the temperature distribution in a volumetric receiver. Sol. Energy 66, 355–369.

Irfan, M. a., Chapman, W., 2009. Thermal stresses in radiant tubes due to axial, circumferential and radial temperature distributions. Appl. Therm. Eng. 29, 1913–1920.

Lata, J.M., Alcalde, S., Fernández, D., Lekube, X., 2010. First surrounding field of heliostats in the world for commercial solar power plants - Gemasolar, in: Proceedings of SolarPACES.

Lipps, F.W., Vant-Hull, L.L., 1978. A cellwise method for the optimization of large central receiver systems. Sol. Energy 20, 505–516.

Modest, M.F., 2003. Radiative heat transfer, Second edition. Academic press, Amsterdam.

Pacheco, J.E., 2002. Final Test and Evaluation Results from the Solar Two Project, SAND2002-0120. Sandia National Laboratories, Albuquerque, NM.

Rodríguez-Sánchez, M.R., Marugan-Cruz, C., Acosta-Iborra, A., Santana, D., 2014a. Comparison of simplified heat transfer models and CFD simulations for molten salt external receiver. Appl. Therm. Eng. 73, 991–1003.

Rodríguez-Sánchez, M.R., Sánchez-González, A., Marugán-Cruz, C., Santana, D., 2015. Flow patterns of external solar receivers. Sol. Energy 122, 940–953.

Rodríguez-Sánchez, M.R., Soria-Verdugo, A., Almendros-Ibáñez, J.A., Acosta-Iborra, A., Santana, D., 2014b. Thermal design guidelines of solar power towers. Appl. Therm. Eng. 63, 428–438.

Salomé, A., Chhel, F., Flamant, G., Ferrière, A., Thiery, F., 2013. Control of the flux distribution on a solar tower receiver using an optimized aiming point strategy: Application to THEMIS solar tower. Sol. Energy 94, 352–366.

Sánchez-González, A., Santana, D., 2015. Solar flux distribution on central receivers: A projection method from analytic function. Renew. Energy 74, 576–587.

Siebers, D.L., Kraabel, J.S., 1984. Estimating convective energy losses from solar central receivers, SAND84-8717. Sandia National Laboratories, Livermore, CA.

Vant-Hull, L.L., 2002. The Role of "Allowable Flux Density" in the Design and Operation of Molten-Salt Solar Central Receivers. J. Sol. Energy Eng. 124, 165.

Vant-Hull, L.L., 2012. Central tower concentrating solar power (CSP) systems, in: Concentrating Solar Power Technology: Principles, Developments and Applications. Woodhead Publishing.

Young, W.C., Budynas, R.G., 2002. Roark's formulas for stress and strain. McGraw-Hill, New York.

Zavoico, A.B., 2001. Solar power tower: Design basis document SAND2001-2100. Sandia National Laboratories, Albuquerque, NM.